Editors' Suggestion

Weyl nodal-line surface half-metal in $CaFeO_3$

Run-Wu Zhang,[1] Da-Shuai Ma,[1] Jian-Min Zhang,[2] and Yugui Yao[1,*]

[1]*Key Laboratory of Advanced Optoelectronic Quantum Architecture and Measurement (MOE), Beijing Key Laboratory of Nanophotonics & Ultrafine Optoelectronic Systems, and School of Physics, Beijing Institute of Technology, Beijing 100081, China*

[2]*Fujian Provincial Key Laboratory of Quantum Manipulation and New Energy Materials, College of Physics and Energy, Fujian Normal University, Fuzhou 350117, China*

(Received 7 January 2021; accepted 20 April 2021; published 7 May 2021)

Manipulating the spin degrees of freedom of electrons affords an excellent platform for exploring novel quantum states in condensed-matter physics and material science. Based on first-principles calculations and analysis of crystal symmetries, we propose a fully spin-polarized composite semimetal state, which is combined with the 1D nodal lines and 2D nodal surfaces, in the half-metal material $CaFeO_3$. In the nodal line-surface half-metal, the Baguenaudier-like nodal lines feature six rings linked together, which are protected by the three independent symmetry operations: $\mathcal{PT}$, $\mathcal{M}_y$, and $\widetilde{\mathcal{M}}_z$. Near the Fermi level, 2D nodal surfaces with fully spin-polarized are guaranteed by the joint operation $\mathcal{TS}_{2i}$ in the $k_{i(i=x,y,z)} = \pi$ plane. Furthermore, high-quality $CaFeO_3$ harbors ultraclean energy dispersion, which is rather robust against strong hydrostatic compressional strain and correlation effect. The realization of the Weyl nodal line-surface half-metal presents great potential for spintronics applications with high-speed and low-power consumption.

DOI: 10.1103/PhysRevB.103.195115

I. INTRODUCTION

Spintronics is considered a rapidly developing field, using electron spin instead of its charge act as a go-between for data storage and transfer, and has attracted extensive interest in recent research [1,2]. Among proposed new spintronic states [3–11], half-metals manifesting 100% spin polarization are regarded as excellent candidates for promoting spin generation, injection, and transport [12]. Particularly, it is a promising route that the electronic band structure of one spin channel exhibits symmetry-protected band crossings near the Fermi level in a half-metal, then the semimetal states would be fully spin-polarized. The fully spin-polarized semimetals are characterized by the coexistence of topological and magnetic features. The search for desirable physical phenomena, such as fully spin-polarized fermion and topological order, could enable the realization of novel quantum devices and is therefore at the forefront of material science.

Akin to band structures of nonmagnetic semimetals, nodal semimetals in half-metals fall into different categories via the dimensionality of the band crossing, including zero-dimensional (0D) nodal points, 1D nodal loops, and 2D nodal surfaces, which makes the classification resemble nonmagnetic semimetals in 3D systems [13–36]. In 0D systems, Weyl nodal points in half-metals are characterized by the separated twofold degenerate points in the Brillouin zone (BZ) and can lead to a Fermi arc on a certain surface. In contrast to 0D nodal points, 1D nodal loops with drumhead surface states in fully spin-polarized materials provide more platforms for novel nodal semimetals. Recent advances in the magnetic semimetal family offered a tremendous boost to the emerging field of topological semimetals in half-metals [37–51]. Such a state was recently predicted for $Li_3(FeO_3)_2$ [41], which presents two fully spin-polarized nodal loops. Compared with Weyl nodal points and nodal loops in half-metal materials, the candidates of Weyl nodal surface half-metals [36] are far fewer, and there is no associated experimental observation yet. An interesting question naturally arises of whether concrete materials can be realized to host both nodal surface and half-metal features. These materials are promising candidates for high-performance spin-based quantum devices in future.

Thus far, most materials with semimetallic characteristics are often suboptimal and suffer from various drawbacks. According to experimental studies and applications, the nontrivial band crossing located far away from the Fermi level and entangled with other irrelevant trivial bands, as well as the complex materials, are hard to implement experimentally, strongly limiting their applicability to high-efficiency nano-spintronics devices. The evolution of semimetals from nonmagnetic to magnetic systems provides a brand-new platform to explore such intriguing physical properties. Therefore, seeking realistic desired semimetal in half-metals with fully spin-polarized fermion will greatly refresh the designs of potential spintronic devices.

Overcoming aforementioned shortcomings, herein, based on first-principles calculations and analysis of crystal symmetries, we propose and characterize a new Weyl nodal line-surface features in half-metal $CaFeO_3$. The $CaFeO_3$ shares a ferromagnetic (FM) ground state and generates 100% spin polarization. The electronic states of spin-up channel manifest remarkable semimetal traits: (i) The fully spin-polarized nodal lines resemble the Baguenaudier toy, which is composed of six nodal rings. These nodal lines are protected

*ygyao@bit.edu.cn

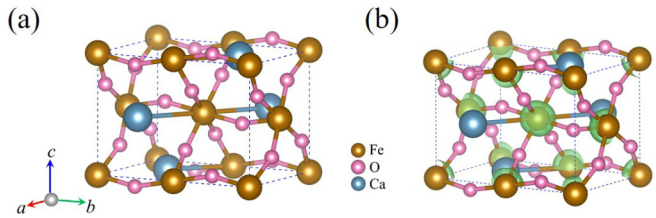

FIG. 1. (a) The crystal structure and (b) the 3D magnetic charge density of $CaFeO_3$. Note: Gold, pink, and light blue colors stand for iron, oxygen, and calcium atoms, respectively.

by the space-time inversion ($\mathcal{PT}$) and mirror ($\mathcal{M}_y$), as well as glide mirror ($\widetilde{\mathcal{M}}_z$) symmetries; (ii) the fully spin-polarized nodal surfaces appeared on the $k_{i(i=x,y,z)} = \pi$ plane near the Fermi level, dictated by the combination of nonsymmorphic twofold screw-rotational and time-reversal symmetries ($\mathcal{TS}_{2i}$). The nodal line-surface in half-metal is mainly derived from the orbitals of light elements, which is very robust against such tiny spin-orbit coupling (SOC). Moreover, the topological nodal line-surface of $CaFeO_3$ can be effectively tailored by hydrostatic compressional strain and correlation effect. It is noteworthy that high-quality $CaFeO_3$ has been synthesized and possesses great application potential [52–54]. Thus, our results offer a realistic material platform for the exploration of the Weyl nodal line-surface half-metal.

II. COMPUTATIONAL METHOD AND CRYSTAL STRUCTURE

To systematically study the electronic properties of $CaFeO_3$, we perform the first-principles calculations by using the Vienna Ab initio Simulation Package (VASP) based on the generalized gradient approximation in the Perdew-Burke-Ernzerhof (PBE) [55,56]. To obtain accurate crystalline structures of $CaFeO_3$, the advanced van der Waals density functional (i.e., SCAN+rVV10 [57]) is performed. In this work, the plane-wave cutoff energy is set as 560 eV, and Γ-centered k-mesh with size $10 \times 7 \times 10$ is used for the primitive cell. To check the correlation effects of the transition metal iron atom, the DFT+U method [58,59] is carried out for calculating the band structures.U values between 3 and 7 eV have been tested for the Fe 3d orbitals. Here, the U value is taken to be 4 eV, which is typical for Fe atom. Moreover, we construct the maximally localized Wannier functions (MLWFs) by employing the WANNIER90 code [60]. The corresponding surface states of nodal line half-metal are implemented with the WannierTools package [61] based on Green's functions method.

The $CaFeO_3$ compound manifests the ABO_3 perovskite structure and usually crystallizes in ample phases under different experimental temperature circumstances such as the orthorhombic phase and the monoclinic phase. At 300 K, similar to the crystal structure of gadolinium orthoferrite ($GdFeO_3$) [54], $CaFeO_3$ is distorted from the ideal cubic perovskite crystal by the same octahedral tilting distortion, as illustrated in Fig. 1(a). To optimize the orthorhombic phase $CaFeO_3$ more precisely, the advanced SCAN+rVV10 method is adopted. The calculated detailed structural parameters are summarized in Table I. Hence, we take the optimized lattice structure by the SCAN+rVV10 method to further explore the electronic property. Remarkably, the optimized lattice parameters of $CaFeO_3$ are in excellent agreement with the experimental result [54]. Furthermore, the Ca atoms occupy the 4c (0.5355, 0.7500, 0.9938) Wyckoff position, Fe atoms occupy the 4a (0.0, 0.0, 0.0) position, and O_1 atoms are at 8d (0.7152, 0.0348, 0.2148), as well as O_2 atoms at 4c (0.5118, 0.2500, 0.5668).

TABLE I. The lattice constants of the crystal $CaFeO_3$ (in unit of Å) are calculated based on the PBE and SCAN+rVV10 methods. The structural parameters of $CaFeO_3$ computed by the SCAN+rVV10 method are very close to the experimental results.

Phase	Experiment [54] $a \setminus b \setminus c$	PBE $a \setminus b \setminus c$	SCAN + rVV10 $a \setminus b \setminus c$
Pnma	5.35 \ 7.50 \ 5.32;	5.43 \ 7.59 \ 5.36;	5.33 \ 7.50 \ 5.31

III. MAGNETIC GROUND STATES AND ELECTRONIC STRUCTURES

In the orthorhombic phase $CaFeO_3$, the 3d transition metal element Fe contributes the magnetic property, which is further verified by performing the 3D magnetic charge density, as shown in Fig. 1(b). Notably, all magnetic moments are localized around Fe atoms, which indicates that these Fe atoms can induce the magnetic property of $CaFeO_3$. Identifying the magnetic ground state of $CaFeO_3$ motivates us to explore the desirable properties. To check the magnetic ground states, we investigate four different kinds of possible magnetic orders, including FM and three antiferromagnetic (AFM1, AFM2, and AFM3) configurations (see details in Appendix A). Consistent with earlier advances on the magnetic structure of $CaFeO_3$ [62–64], our calculations indicate that the FM state possesses the lowest total energy among all possible magnetic states, meaning that the FM ground states are preferred. The magnetic moment is found to be 16 μ_B per primitive cell, which is mainly contributed by the four Fe atoms.

From the projected density of states for FM order $CaFeO_3$, one notes that the $CaFeO_3$ behaves as a half-metallic state with spin-up channel possessing metallic, while the spin-down channel keeps semiconducting, as displayed in Fig. 2(a). Considering the spin-polarized calculation, the band structure shows that the band-crossing features around the Fermi energy are fully spin-polarized in the spin-up channel, while the spin-down channel exhibits a large gap of about 1.30 eV. The energy range of the spin-down channel is sufficient to overcome the interruption of irrelevant bands, therefore making ideal half-metals with fully spin-polarized. Moreover, the orbital-projection analysis shows that the obvious contributions to the conduction band minimum (CBM) and the valence band maximum (VBM) near the Fermi level are mainly dominated by the Fe 3d (d_{xz} and $d_{x^2-y^2}$) and O 2p orbitals, as plotted in Fig. 2(b), which agrees well with previous studies [63].

Buoyed by the attractive properties of half-metals and semimetals, we plot a new quantum state of matter, termed the Weyl nodal line-surface half-metal, which enjoys both the

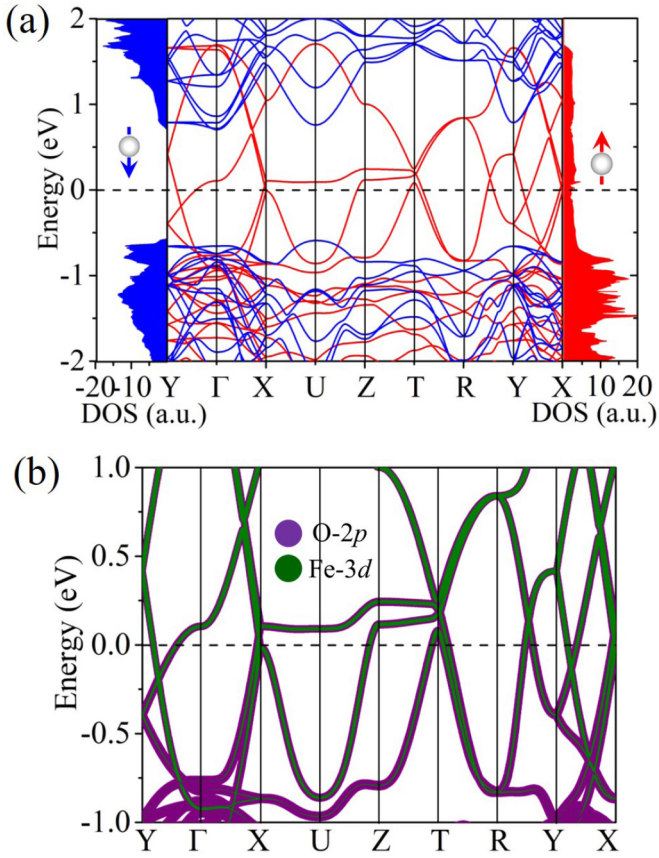

FIG. 2. Spin-resolved band structure and the density of state of (a) $CaFeO_3$. Orbital-projected band structure of spin-up channel for (b) $CaFeO_3$ contributed by O-2p and Fe-3d (d_{xz} and $d_{x^2-y^2}$) orbitals. Note: the red and blue arrows represent spin-up and spin-down channels, respectively.

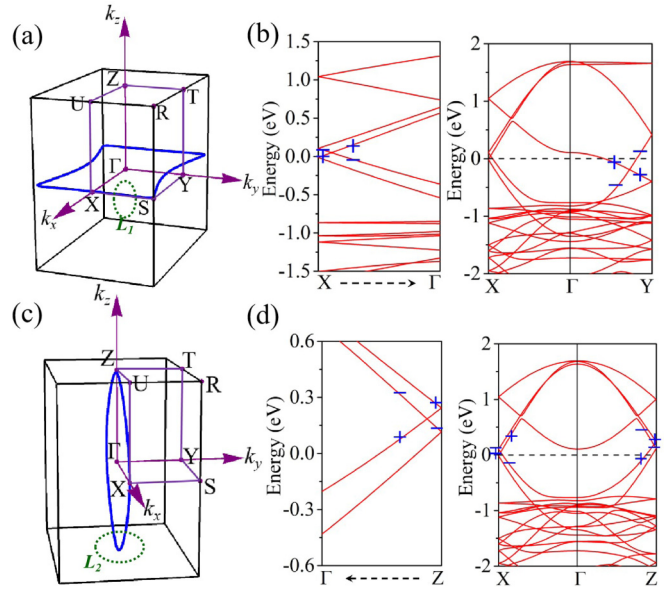

FIG. 3. The 3D profile of the nodal lines lie on the (a) $k_z = 0$ plane and the (c) $k_y = 0$ plane, respectively. Band structures of spin-up channel for $CaFeO_3$ along the X-Γ-Y path and X-Γ-Z path. The eigenvalues of $\widetilde{\mathcal{M}}_z$ and $\mathcal{M}_y$ symmetry operators for each band are labeled + and − in the enlarged band structures (b) and (d). The green dashed lines labeled L_1 and L_2 represent two respective loops along which the Berry phase is calculated. The topological protection of nodal lines is further checked by directly calculating the nontrivial π Berry phase along two small loops (L_1 and L_2) enclosing the nodal lines.

half-metal and the semimetal traits, with fully spin-polarized Weyl fermions around Fermi level formed in a single spin channel. Via an enlarged view of the low-energy band structure in Fig. 2(b), $CaFeO_3$ exhibits band crossing and band degeneracy: (i) The band crossings appear on the Y-Γ-X paths near the Fermi level; (ii) the bands are doubly degenerate along the high-symmetry X-U-Z-T paths. Before proceeding, it is notable that spin is a good quantum number in spin-polarized systems, and all Bloch states of spin and orbital can be reduced to two orthogonal subspaces in different spin channels [65,66]. By choosing the axis along the spin polarization, the two spin channels are decoupled, which in turn preserve the crystal symmetries for the single spin channel. In the following, we further explore these charming phenomena.

IV. WEYL NODAL LINE-SURFACE STATES

Regarding the space group *Pnma* in $CaFeO_3$, it is important to note the presence of the following symmetry operation: The inversion $\mathcal{P}$, mirror reflection $\mathcal{M}_y : (x, y, z) \to (x, -y + \frac{1}{2}, z)$, two glide mirror reflections $\widetilde{\mathcal{M}}_x : (x, y, z) \to (-x + \frac{1}{2}, y + \frac{1}{2}, z + \frac{1}{2})$, and $\widetilde{\mathcal{M}}_z : (x, y, z) \to (x + \frac{1}{2}, y, -z + \frac{1}{2})$, as well as three twofold screw rotations $\mathcal{S}_{2x} : (x, y, z) \to (x + \frac{1}{2}, -y + \frac{1}{2}, -z + \frac{1}{2})$, $\mathcal{S}_{2y} : (x, y, z) \to (-x, y + \frac{1}{2}, -z)$, and $\mathcal{S}_{2z} : (x, y, z) \to (-x + \frac{1}{2}, -y, z + \frac{1}{2})$. We first consider the linear band-crossings features of $CaFeO_3$ along the X-Γ-Y path on the $k_z = 0$ plane. As depicted in Fig. 3(a), we perform a scan of the momentum distribution for these band crossings and observe a continuous nodal line lie exactly on the $k_z = 0$ plane, demonstrating these crossing points are not isolated. In Fig. 3(b), the CBM and VBM have opposite signs of the eigenvalues of $\widetilde{\mathcal{M}}_z$ concerning the $k_z = 0$ plane, indicating the gapless nodal line is protected by the $\widetilde{\mathcal{M}}_z$ symmetry. A similar analysis also can be applied to the $k_y = 0$ plane, as plotted in Figs. 3(c) and 3(d). Therefore, two mutually perpendicular nodal lines in $CaFeO_3$ are exactly lying on the two mirror invariant planes ($k_y = 0$ and $k_z = 0$). Moreover, through careful scanning calculation, we reveal that the trace of the band crossings actually forms snakelike nodal lines (not necessary to lie on the mirror invariant planes), as illustrated in Fig. 4(a). Analogous to alkaline-earth compounds [15], such snakelike nodal lines are protected by $\mathcal{PT}$ symmetry. To further validate the topological properties of $CaFeO_3$, we introduce the Berry phase calculation along with distinctive lines. We find that Berry phase equals to π along a ring L_1 (L_2 and L_3) threading the nodal lines located on the $\mathcal{M}_y$, $\widetilde{\mathcal{M}}_z$ as well as snakelike lines. Noticeably, due to these topological nodal lines derived from a single spin channel, these low-energy nodal-line fermions behave as fully spin-polarized features, which will be useful for spintronics applications.

Unique fully spin-polarized nodal lines of $CaFeO_3$ inspire us to further explore potential applications. To directly

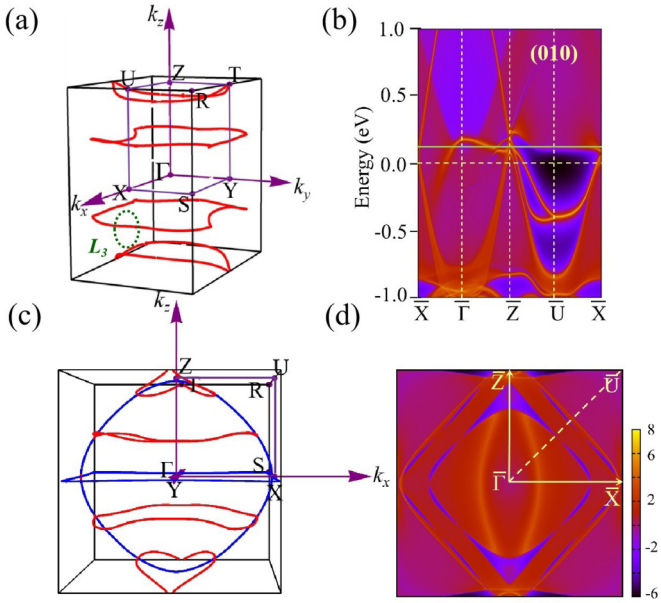

FIG. 4. (a) The 3D view of the snakelike nodal lines in the BZ. The calculated Berry phase of an arbitrary green dashed ring (i.e., L_3) intersecting a snakelike nodal line. (b) The projected surface states for the (010) plane. (c) The *xoz* perspective of the nodal line profiles in the BZ. (d) The isoenergy ($E_f = 0.1$ eV) surface around the $\bar{\Gamma}$ point for the (010) plane.

present the intriguing properties of topological nodal lines, the hallmark drumheadlike surface states are performed. Figure 4(b) shows the surface spectrum for the (010) plane. Significantly, the drumheadlike state along $\bar{Z}$-$\bar{U}$-$\bar{X}$ presents dispersive, which is effected by the specific surface condition. We can change the surface termination or passivate the surface to change the dispersion. As for Fig. 4(c), we plot the nodal line profiles in the *xoz* perspective. These nodal lines feature a large loop interlinked with other small loops and each has a clear track, which is very similar to the Baguenaudier toy. The isoenergy band contour of the surface at the (010) plane is obtained in Fig. 4(d), which is basically consistent with the case of Fig. 4(c) (the constant energy slice at $E_f = 0.1$ eV). More importantly, the 2D nearly flat drumheadlike surface states in nodal line half-metals not only have a large density of states but also are fully spin-polarized, which provide a good playground for spintronics [1,2], topological superconductivity [67,68], and topological catalysts [69,70].

Moreover, the bulk band structures of $CaFeO_3$ present 2D fully spin-polarized nodal surface characteristics. In the absence of SOC, the spin and orbital degrees of freedom are decoupled, such that each spin channel can be considered in the subspace. Considering the spin polarization, we first discuss the degeneracy along the X-S-R-U-X path, as seen in Fig. 5(a). The twofold screw rotation $\mathcal{S}_{2x} : (x, y, z) \rightarrow (x + \frac{1}{2}, -y + \frac{1}{2}, -z + \frac{1}{2})$, which is a nonsymmorphic symmetry involving a half translation along the rotation axis. In momentum space, $\mathcal{S}_{2x}$ inverses k_y and k_z while it preserves k_x. One finds that $(\mathcal{S}_{2x})^2 = T_{100} = e^{-ik_x}$, where T_{100} is the translation along the x-direction by a lattice constant. $\mathcal{T}$ is antiunitary and inverses k with $\mathcal{T}^2 = 1$. Thus, $\mathcal{T}\mathcal{S}_{2x}$ is antiunitary and only inverses k_x. Since $[\mathcal{T}, S_{2x}] = 0$, $\mathcal{T}\mathcal{S}_{2x}$ satisfies $(\mathcal{T}\mathcal{S}_{2x})^2$

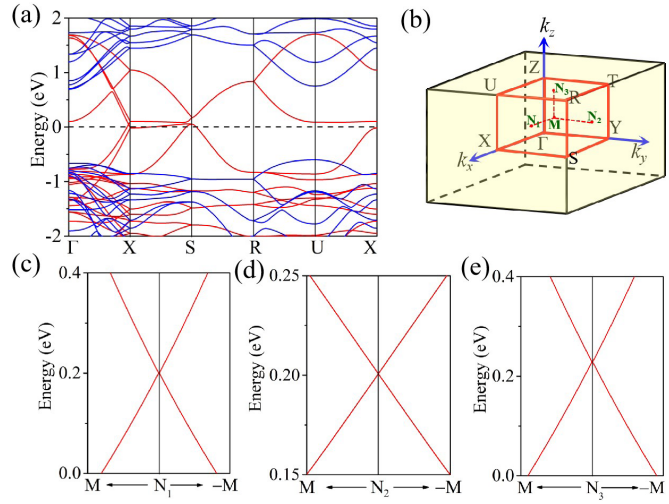

FIG. 5. (a) Spin-resolved band structure of $CaFeO_3$. (b) The corresponding BZ. Note: M is the middle point of the Γ-R path and N_1 (N_2 and N_3) is the middle point of the X-R (Y-R and Z-R) path. Enlarged band dispersion along the M and N_1 (c) [N_2 (d) and N_3 (e)] path showing the linear crossing between two bands along the k_x (k_y and k_z) direction.

$= e^{-ik_x}$. When $k_x = \pi$, each k point is invariant under the $\mathcal{T}\mathcal{S}_{2x}$ operation, and $(\mathcal{T}\mathcal{S}_{2x})^2 = -1$ means that there is a Kramers-like degeneracy due to the antiunitary $\mathcal{T}\mathcal{S}_{2x}$ symmetry. Thus, the bands in the $k_x = \pi$ plane must be doubly degenerate, forming the nodal surface. A similar argument has been proposed in the previous discussion of the material $CsCrI_3$ [36]. Moreover, in Fig. 5(c), we check the dispersion along a generic k-path M-N_1, which is not a high-symmetry path [see Fig. 5(b)]. The linear crossing can be obtained from the generic path, which further proved the existence of nodal surface states. It is notable that the symmetry requires the presence of the nodal surface and confines the location of the

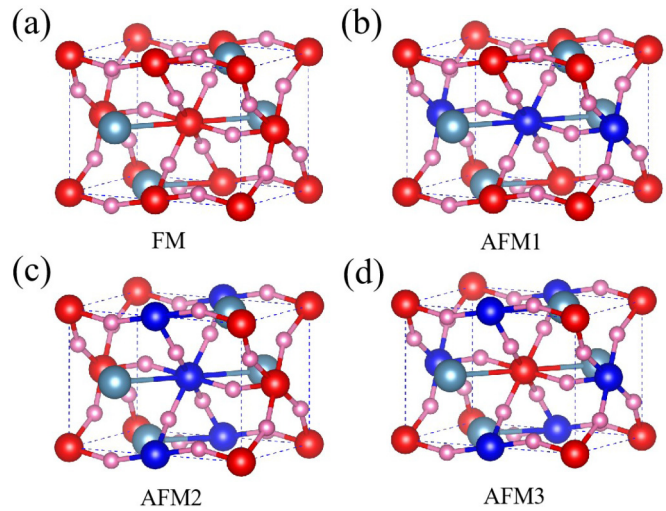

FIG. 6. Schematics of four different magnetic structures (a) FM, (b) AFM1, (c) AFM2, and (d) AFM3 for $CaFeO_3$. The red atoms stand for the spin-up direction and the blue atoms stand for the spin-down direction.

TABLE II. Relative energies (in eV/unit cell) for FM, AFM1, AFM2, and AFM3 states of $CaFeO_3$ ($U = 3\sim7$ eV).

U values (eV)	FM	AFM1	AFM2	AFM3
3	0	0.74443	0.33124	1.01202
4	0	0.77705	0.35202	1.11284
5	0	0.77984	0.35955	1.18495
6	0	0.76033	0.35854	1.21688
7	0	0.71583	0.34933	1.18635

nodal surface in the $k_x = \pi$ plane. It puts no constraint on the energy and the dispersion of the nodal surface. For the nodal surface state in $k_x = \pi$ plane, the location of the energy dispersion is very close to the Fermi level. Similar to the case of $k_x = \pi$ plane, the nodal surface states can be revealed in the $k_y = \pi$ and $k_z = \pi$ planes [71]. The protection mechanisms of the other two nodal surfaces are consistent with the first one, and similar features are plotted in Figs. 5(d) and 5(e).

V. DISCUSSION AND CONCLUSION

Considering the correlation effects of the transition metal d orbitals, we perform the GGA+U calculations by taking into account the on-site Coulomb interaction and find that the nodal line and nodal surface states are stable within U values (from 3 to 7 eV). It is also stable against a wide range of strains. The details are presented in the Appendixes. Thus, such nodal line-surface is robust against correlation and strain effects.

In conclusion, we identify that $CaFeO_3$ hosts the fully spin-polarized nodal line-surface characteristic. The FM ground state of $CaFeO_3$ is half-metal and features nodal line-surface in the spin-up channel. The fully spin-polarized nodal lines possess Baguenaudier-like rings due to the $\mathcal{PT}$, $\mathcal{M}_y$, and $\widetilde{\mathcal{M}}_z$ symmetries with negligible SOC. Moreover, the drumheadlike fully spin-polarized surface states are obtained. Also, the bulk band structures of $CaFeO_3$ hold unique 2D nodal surface with fully spin-polarized as protected by joint operation $\mathcal{TS}_{2i}$ at the $k_{i(i=x,y,z)} = \pi$ plane. To our knowledge, such coexistence of the spin-polarized 1D nodal line and the 2D nodal surface is different from the current proposed nodal line or surface in nonmagnetic systems, and this unique candidate may have great potential in future spintronics applications.

ACKNOWLEDGMENTS

This work is supported by the National Natural Science Foundation of China (Grants No. 12047512, 11734003, 12061131002), the National Key R&D Program of China (Grants No. 2020YFA0308800, No. 2016YFA0300600), and the Strategic Priority Research Program of Chinese Academy of Sciences (Grant No. XDB30000000). R.W.Z. also acknowledges the support from the Project Funded by China Postdoctoral Science Foundation (Grant No. 2020M680011).

R.W.Z and D.S.M. contributed equally to this work.

APPENDIX A: FOUR DIFFERENT MAGNETIC CONFIGURATIONS OF $CaFeO_3$

Considering the iron (Fe)-based materials, the magnetic property is generally attributed to the Fe atoms. To determine the magnetic ground states of $CaFeO_3$, we calculate the total energy of four different magnetic configurations, including FM and three anti-FM (AFM1, AFM2, and AFM3) configurations, which are shown in Fig. 6. Moreover, we found that the FM ground states of $CaFeO_3$ are robust against the variation in U from 3 to 7 eV; see the details in Table II.

APPENDIX B: A MINIMAL EFFECTIVE HAMILTONIAN TO COMPREHEND THE WEYL NODAL LINE-SURFACE STATES

Here, we introduce a minimal effective Hamiltonian to realize the Weyl nodal line-surface half-metal. As discussed in Section IV, the model yields the symmetries $\widetilde{\mathcal{M}}_x$, $\mathcal{M}_y$, and $\widetilde{\mathcal{M}}_z$. We consider spin-full p_z orbitals located at the $4c$ Wyckoff position. Then, we get the eight-band Hamiltonian as follows,

$$H(k) = \begin{pmatrix} 0 & t_1 f(k_y) g*(k_x + k_z) & 0 & t_2 f^*(k_x) \\ t_1 f^*(k_y) g(k_x + k_z) & 0 & t_2 f(k_x) & 0 \\ 0 & t_2 f^*(k_x) & 0 & t_1 f^*(k_y) \\ t_2 f(k_x) & 0 & t_1 f(k_y) & 0 \end{pmatrix} \otimes s_0 + \Delta I_4 s_z, \tag{B1}$$

where $f(k) = 1 + \cos(k) + i \sin(k)$, $g(k) = f(k) - 1$, s_z is the Pauli matrix representing the spin degree of freedom, Δ is the onsite energy of the electron with spin-up channel and is nonzero in magnetic systems, and $t_{1,2}$ is considered hopping. For $k_x = \pi$ plane, the eigenvalues of the spin-up channel are $\Delta \pm \sqrt{2} t_1 \sqrt{1 + \cos(k_y)}$, resulting in two double-degenerated bands, nodal surface. The eigenvalues of the spin-up channel is $\Delta \pm \sqrt{2} t_2 \sqrt{1 + \cos(k_x)}$ and $\Delta \pm \sqrt{2}\sqrt{t_1^2 + t_2^2 + t_2^2 \cos(k_x) + t_1^2 \cos(k_y)}$ in $k_y = \pi$ and $k_z = \pi$ planes, respectively. Thus, we get the nodal surface, as illustrated in Fig. 7(a).

Moreover, we can also get the nodal line in $k_x = 0$ plane, as shown in Fig. 7(b). Along the high-symmetry line $\Gamma \rightarrow$X or $\Gamma \rightarrow$Y, the energy eigenvalues of the two bands near the Fermi level are $\pm 2[-t_1 + t_2 \cos(k_x/2)]$ or $\pm 2[-t_2 + t_1 \cos(k_y/2)]$.

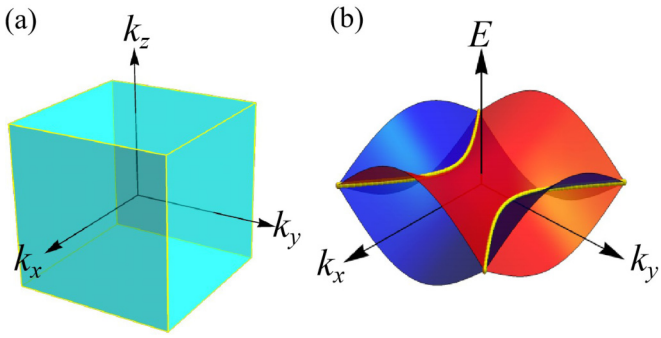

FIG. 7. (a) Schematic of the nodal surface. The bands in $k_{i(i=x,y,z)} = \pi$ planes, highlighted in cyan, are double degenerate. (b) The 3D band structure with $t_1 = 0.5$ and $t_2 = 0.4$. Here only the two bands near the Fermi level are shown. There is a nodal line, highlighted by the yellow line, centering on the Y point.

Thus, if $t_1 > t_2 (t_1 < t_2)$, there is a band crossing along $\Gamma \rightarrow$Y ($\Gamma \rightarrow$X), while the mirror eigenvalue of $\widetilde{\mathcal{M}}_z$ at Γ of the highest occupied valence band is opposite with that at Y(X). Thus, there is a nodal line centering on the Y(X) point.

APPENDIX C: BAND STRUCTURES WITH HUBBARD U CORRECTION

Concerning the correlation effect of $3d$ transition metal element Fe in $CaFeO_3$, in our calculation, we have set the Hubbard value with $U = 4$ eV (a representative empirical value for Fe $3d$ orbitals) and verified that $CaFeO_3$ hosts Weyl nodal line-surface half-metal states with fully spin-polarized near the Fermi level. Moreover, we have checked a series of reasonable U values (from 3 to 7 eV). It is observed that the key band features such as the character of spin-up channel are well preserved against the variation in U values, and the main difference is that the gap for the spin-down channel is increased from 0.98 to 2.01 eV, as plotted in Fig. 8. From an overall perspective, the system is robust against the various U values, and the low-energy band features are very similar to the result of $U = 4$ eV.

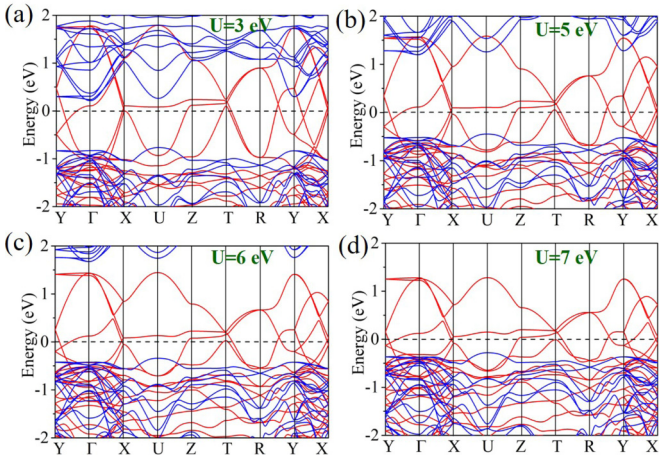

FIG. 8. Spin-resolved band structures of $CaFeO_3$ in the absence of SOC effects for (a) $U = 3$ eV, (b) $U = 5$ eV, (c) $U = 6$ eV, and (d) $U = 7$ eV. Red and blue lines represent spin-up and spin-down channels, respectively.

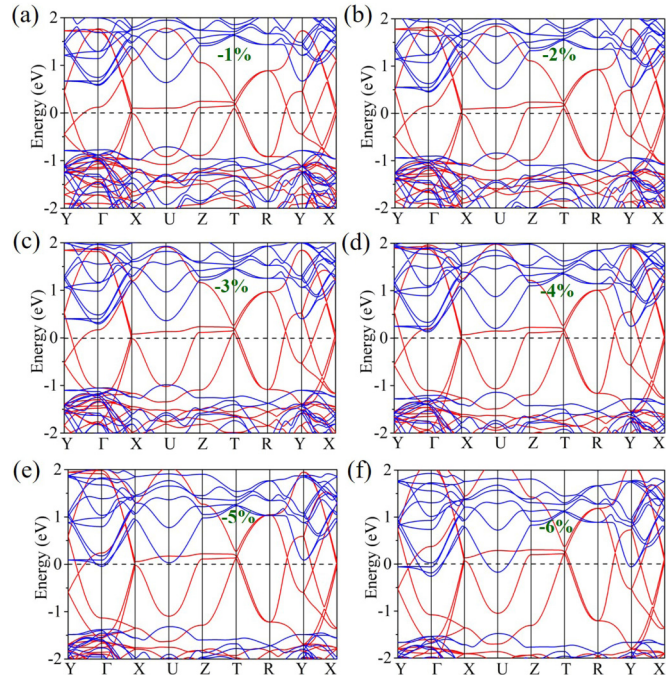

FIG. 9. Spin-resolved band structures of $CaFeO_3$ ($U = 4$ eV) with different hydrostatic compressional strains for (a) -1%, (b) -2%, (c) -3%, (d) -4%, (e) -5%, and (f) -6% are calculated.

APPENDIX D: HYDROSTATIC STRAIN EFFECTS ON $CaFeO_3$

We further explore the robustness of the Weyl nodal line-surface half-metal and application feasibility of $CaFeO_3$. Simulating the real condition, we utilize small perturbations (e.g., external hydrostatic strain) for tuning electronic properties in practice. All crossing features of $CaFeO_3$ under such a wide range of hydrostatic compressional strains (from -6% to -1%) still exist as expected, harboring the robustness of fully spin-polarized nodal line-surface against certain structural deformation, as illustrated in Fig. 9. By increasing the hydrostatic compressional strains, the band structures of spin-up channel are almost similar to the ones of ground state $CaFeO_3$. The main difference is that the gaps for the spin-down channel are increased, while the crossing characters for the spin-up channel remain. These valuable findings are very beneficial for future experimental preparation and make $CaFeO_3$ highly adaptable to various application environments.

TABLE III. Total energy per primitive cell (in μeV, relative to that of the $FM_{[100]}$ ground state). The values are calculated by the GGA+SOC method with $U = 4$ eV.

$FM_{[100]}$	$FM_{[010]}$	$FM_{[001]}$	$FM_{[110]}$	$FM_{[101]}$	$FM_{[011]}$	$FM_{[111]}$
0	110	40	70	10	90	60

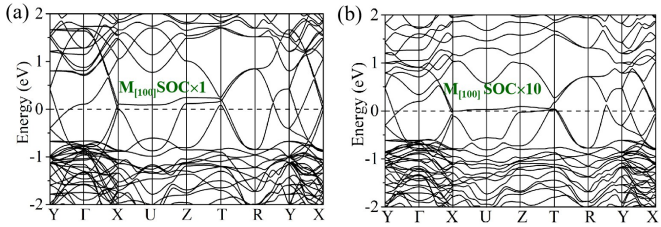

FIG. 10. (a) Calculated band structure of $CaFeO_3$ ($U = 4$ eV) with SOC. (b) Band structure of $CaFeO_3$ after artificially increasing the intrinsic SOC by 10 times.

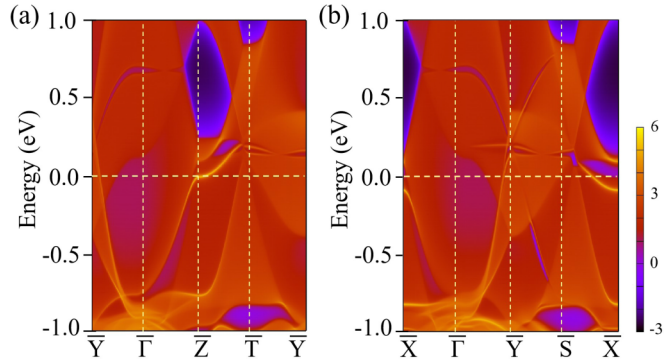

FIG. 11. The projected surface states of $CaFeO_3$ for (a) the (100) and (b) the (001) planes.

APPENDIX E: DISCUSSIONS FOR $CaFeO_3$ IN THE PRESENCE OF SOC

Regarding the FM ground states of $CaFeO_3$, we consider seven possible orientations for the magnetic moments, namely, the [100], [010], [001], [110], [101], [011], and [111] directions. Among these possible states, our calculations show that the lowest energy is the $FM_{[100]}$ configuration, as shown in Table III.

Here we discuss the effect of SOC. Besides the $\mathcal{P}$ in space group *Pnma*, the symmetric operators of the system mainly include the three $\mathcal{S}_{2i}$, $\mathcal{M}_y$, $\widetilde{\mathcal{M}}_x$, and $\widetilde{\mathcal{M}}_z$. For the FM [100] as the ground-state configuration and that the magnetization direction parallels to $\widetilde{\mathcal{M}}_x$, only $\widetilde{\mathcal{M}}_x$ symmetry survives, and all the nodal lines and nodal surfaces will be broken. When the magnetization direction parallels to the normal direction of the $\mathcal{M}_y$ or $\widetilde{\mathcal{M}}_z$, the nodal line will survive because the corresponding mirror or glide mirror symmetry is preserved.

Although all the nodal lines and nodal surfaces will have gaped under the FM [100] as the ground-state configuration, the outline of the nodal lines is kept, i.e., most of the four nodal rings are opened by SOC with a gap of less than 26 meV. To demonstrate the above result, we present the DFT band structure with SOC in Fig. 10. One can see that the band structure is virtually unaffected under the SOC, as shown in Fig. 10(a). Even with artificially increasing the intrinsic SOC by 10 times, the size of the gap increases accordingly and far less than the energy scale of room temperature (26 meV), as plotted in Fig. 10(b). For these reasons, the SOC effect of $CaFeO_3$ can be safely neglected and is irrelevant here.

APPENDIX F: SURFACE STATES OF $CaFeO_3$ FOR THE (100) AND (001) PLANES

To more comprehensively present the topological drumheadlike surface properties of nodal lines, we introduce the projected surface states of $CaFeO_3$ for the (100) and (001) planes. As plotted in Figs. 11(a) and 11(b), the projected surface states for the (100) and (001) planes are obtained, where surface bands are visible. Interestingly, the drumheadlike surface states are nearly flat with small dispersion, which indicates a high density of states around the Fermi level.

[1] S. A. Wolf, D. D. Awschalom, R. A. Buhrman, J. M. Daughton, S. von Molnár, M. L. Roukes, A. Y. Chtchelkanova, and D. M. Treger, Science **294**, 1488 (2001).

[2] I. Žutić, J. Fabian, and S. Das Sarma, Rev. Mod. Phys. **76**, 323 (2004).

[3] R. A. de Groot, F. M. Mueller, P. G. van Engen, and K. H. J. Buschow, Phys. Rev. Lett. **50**, 2024 (1983).

[4] H. van Leuken and R.A. de Groot, Phys. Rev. Lett. **74**, 1171 (1995).

[5] H. Ohno, A. Shen, F. Matsukura, A. Oiwa, A. Endo, S. Katsumoto, and Y. Iye, Appl. Phys. Lett. **69**, 363 (1996).

[6] X. Wang, Phys. Rev. Lett. **100**, 156404 (2008).

[7] C. L. Kane and E. J. Mele, Phys. Rev. Lett. **95**, 146802 (2005).

[8] M. König, S. Wiedmann, C. Brüne, A. Roth, H. Buhmann, L. W. Molenkamp, X.-L. Qi, and S.-C. Zhang, Science **318**, 766 (2007).

[9] D. Hsieh, D. Qian, L. Wray, Y. Xia, Y. S. Hor, R. J. Cava, and M. Z. Hasan, Nature (London) **452**, 970 (2008).

[10] X. Wan, A. M. Turner, A. Vishwanath, and S. Y. Savrasov, Phys. Rev. B **83**, 205101 (2011).

[11] C.-Z. Chang, J. Zhang, X. Feng, J. Shen, Z. Zhang, M. Guo, K. Li, Y. Ou, P. Wei, L.-L. Wang *et al.*, Science **340**, 167 (2013).

[12] J.-H. Park, E. Vescovo, H.-J. Kim, C. Kwon, R. Ramesh, and T. Venkatesan, Nature (London) **392**, 794 (1998).

[13] Z. Wang, Y. Sun, X.-Q. Chen, C. Franchini, G. Xu, H. Weng, X. Dai, and Z. Fang, Phys. Rev. B **85**, 195320 (2012).

[14] Z. Wang, H. Weng, Q. Wu, X. Dai, and Z. Fang, Phys. Rev. B **88**, 125427 (2013).

[15] H. Huang, J. Liu, D. Vanderbilt, and W. Duan, Phys. Rev. B **93**, 201114(R) (2016).

[16] T.-R. Chang, S.-Y. Xu, D. S. Sanchez, W.-F. Tsai, S.-M. Huang, G. Chang, C.-H. Hsu, G. Bian, I. Belopolski, Z.-M. Yu *et al.*, Phys. Rev. Lett. **119**, 026404 (2017).

[17] W. Cao, P. Tang, Y. Xu, J. Wu, B.-L. Gu, and W. Duan, Phys. Rev. B **96**, 115203 (2017).

[18] H. Weng, C. Fang, Z. Fang, B. A. Bernevig, and X. Dai, Phys. Rev. X **5**, 011029 (2015).

[19] Y. Sun, S.-C. Wu, M. N. Ali, C. Felser, and B. Yan, Phys. Rev. B **92**, 161107(R) (2015).

[20] A. A. Soluyanov, D. Gresch, Z. Wang, Q. Wu, M. Troyer, X. Dai, and B. A. Bernevig, Nature (London) **527**, 495 (2015).

[21] J. Ruan, S.-K. Jian, D. Zhang, H. Yao, H. Zhang, S.-C. Zhang, and D. Xing, Phys. Rev. Lett. **116**, 226801 (2016).

[22] G. Autes, D. Gresch, M. Troyer, A. A. Soluyanov, and O. V. Yazyev, Phys. Rev. Lett. **117**, 066402 (2016).

[23] M. Ezawa, Phys. Rev. Lett. **116**, 127202 (2016).

[24] S. Li, Z.-M. Yu, Y. Liu, S. Guan, S.-S. Wang, X. Zhang, Y. Yao, and S. A. Yang, Phys. Rev. B **96**, 081106(R) (2017).

[25] J. Wang, Phys. Rev. B **96**, 081107(R) (2017).

[26] R.-W. Zhang, C.-C. Liu, D.-S. Ma, M. Wang, and Y. Yao, Phys. Rev. B **98**, 035144 (2018).

[27] D.-S. Ma, J. Zhou, B. Fu, Z.-M. Yu, C.-C. Liu, and Y. Yao, Phys. Rev. B **98**, 201104(R) (2018).

[28] C. Gong, Y. Xie, Y. Chen, H.-S. Kim, and D. Vanderbilt, Phys. Rev. Lett. **120**, 106403 (2018).

[29] R. Yu, Q. Wu, Z. Fang, and H. Weng, Phys. Rev. Lett. **119**, 036401 (2017).

[30] S.-S. Wang, Y. Liu, Z.-M. Yu, X.-L. Sheng, and S. A. Yang, Nat. Commun. **8**, 1844 (2017).

[31] Z. Yan, R. Bi, H. Shen, L. Lu, S.-C. Zhang, and Z. Wang, Phys. Rev. B **96**, 041103(R) (2017).

[32] X.-L. Sheng, Z.-M. Yu, R. Yu, H. Weng, and S. A. Yang, J. Phys. Chem. Lett. **8**, 3506 (2017).

[33] X. Zhang, Z.-M. Yu, Z. Zhu, W. Wu, S.-S. Wang, X.-L. Sheng, and S. A. Yang, Phys. Rev. B **97**, 235150 (2018).

[34] C. Zhong, Y. Chen, Y. Xie, S. A. Yang, M. L. Cohen, and S. Zhang, Nanoscale **8**, 7232 (2016).

[35] Q.-F. Liang, J. Zhou, R. Yu, Z. Wang, and H. Weng, Phys. Rev. B **93**, 085427 (2016).

[36] W. Wu, Y. Liu, S. Li, C. Zhong, Z.-M. Yu, X.-L. Sheng, Y.X. Zhao, and S. A. Yang, Phys. Rev. B **97**, 115125 (2018).

[37] G. Xu, H. Weng, Z. Wang, X. Dai, and Z. Fang, Phys. Rev. Lett. **107**, 186806 (2011).

[38] Y. Jiao, F. Ma, C. Zhang, J. Bell, S. Sanvito, and A. Du, Phys. Rev. Lett. **119**, 016403 (2017).

[39] Q. Wang, Y. Xu, R. Lou, Z. Liu, M. Li, Y. Huang, D. Shen, H. Weng, S. Wang, and H. Lei, Nat. Commun. **9**, 3681 (2018).

[40] Z. Zhang, Q. Gao, C.-C. Liu, H. Zhang, and Y. Yao, Phys. Rev. B **98**, 121103(R) (2018).

[41] C. Chen, Z.-M. Yu, S. Li, Z. Chen, X.-L. Sheng, and S. A. Yang, Phys. Rev. B **99**, 075131 (2019).

[42] H. Wu, D.-S. Ma, B. Fu, W. Guo, and Y. Yao, J. Phys. Chem. Lett. **10**, 2508 (2019).

[43] X. Zhou, R.-W. Zhang, Z. Zhang, D.-S. Ma, W. Feng, Y. Mokrousov, and Y. Yao, J. Phys. Chem. Lett. **10**, 3101 (2019).

[44] S.-S. Wang, Z.-M. Yu, Y. Liu, Y. Jiao, S. Guan, X.-L. Sheng, and S. A. Yang, Phys. Rev. Mater. **3**, 084201 (2019).

[45] J.-Y. You, C. Chen, Z. Zhang, X.-L. Sheng, S. A. Yang, and G. Su, Phys. Rev. B **100**, 064408 (2019).

[46] R.-W. Zhang, Z. Zhang, C.-C. Liu, and Y. Yao, Phys. Rev. Lett. **124**, 016402 (2020).

[47] E. Liu, Y. Sun, N. Kumar, L. Muechler, A. Sun, L. Jiao, S.-Y. Yang, D. Liu, A. Liang, Q. Xu *et al.*, Nat. Phys. **14**, 1125 (2018).

[48] T. He, X. Zhang, Y. Liu, X. Dai, G. Liu, Z.-M. Yu, and Y. Yao, Phys. Rev. B **102**, 075133 (2020).

[49] H. Zhang, X. Zhang, Y. Liu, X. Dai, G. Chen, and G. Liu, Phys. Rev. B **102**, 195124 (2020).

[50] W. Jiang, H. Huang, F. Liu, J.-P. Wang, and T. Low, Phys. Rev. B **101**, 121113(R) (2020).

[51] H. Zhang, X. Zhang, T. He, X. Dai, Y. Liu, G. Liu, L. Wang, and Y. Zhang, Phys. Rev. B **102**, 155116 (2020).

[52] S. Morimoto, T. Yamanaka, and M. Tanaka, Physica B **237**, 66 (1997).

[53] T. Takeda, R. Kanno, Y. Kawamoto, M. Takano, S. Kawasaki, T. Kamiyama, and F. Izumi, Solid State Sci. **2**, 673 (2000).

[54] P. M. Woodward, D. E. Cox, E. Moshopoulou, A. W. Sleight, and S. Morimoto, Phys. Rev. B **62**, 844 (2000).

[55] J. P. Perdew, K. Burke, and M. Ernzerhof, Phys. Rev. Lett. **77**, 3865 (1996).

[56] P. E. Blöchl, Phys. Rev. B **50**, 17953 (1994).

[57] H. Peng, Z.-H. Yang, J. P. Perdew, and J. Sun, Phys. Rev. X **6**, 041005 (2016).

[58] V. I. Anisimov, J. Zaanen, and O. K. Andersen, Phys. Rev. B **44**, 943 (1991).

[59] S. L. Dudarev, G. A. Botton, S. Y. Savrasov, C. J. Humphreys, and A. P. Sutton, Phys. Rev. B **57**, 1505 (1998).

[60] A. A. Mostofi, J. R. Yates, Y.-S. Lee, I. Souza, D. Vanderbilt, and N. Marzari, Comput. Phys. Commun. **178**, 685 (2008).

[61] Q. Wu, S. Zhang, H.-F. Song, M. Troyer, and A. A. Soluyanov, Comput. Phys. Commun. **224**, 405 (2018).

[62] V. Alexandrov, E. Kotomin, J. Maier, and R. Evarestov, J. Chem. Phys. **129**, 214704 (2008).

[63] A. Cammarata and J. M. Rondinelli, Phys. Rev. B **86**, 195144 (2012).

[64] G. M. Dalpian, Q. Liu, J. Varignon, M. Bibes, and A. Zunger, Phys. Rev. B **98**, 075135 (2018).

[65] G. Chang, S.-Y. Xu, X. Zhou, S.-M. Huang, B. Singh, B. Wang, I. Belopolski, J. Yin, S. Zhang, A. Bansil *et al.*, Phys. Rev. Lett. **119**, 156401 (2017).

[66] Z. Wang, M.G. Vergniory, S. Kushwaha, M. Hirschberger, E.V. Chulkov, A. Ernst, N. P. Ong, R. J. Cava, and B. A. Bernevig, Phys. Rev. Lett. **117**, 236401 (2016).

[67] N. B. Kopnin, T. T. Heikkilä, and G. E. Volovik, Phys. Rev. B **83**, 220503(R) (2011).

[68] G. Volovik, Phys. Scr. **2015**, 014014 (2015).

[69] C. R. Rajamathi, U. Gupta, N. Kumar, H. Yang, Y. Sun, V. Süß, C. Shekhar, M. Schmidt, H. Blumtritt, P. Werner *et al.*, Adv. Mater. **29**, 1606202 (2017).

[70] J. Li, H. Ma, Q. Xie, S. Feng, S. Ullah, R. Li, J. Dong, D. Li, Y. Li, and X.-Q. Chen, Sci. China Mater. **61**, 23 (2018).

[71] Z.-M. Yu, W. Wu, Y.X. Zhao, and S. A. Yang, Phys. Rev. B **100**, 041118(R) (2019).